SANDIA REPORT

SAND2009-0521
Unlimited Release
Printed Month 2009

Thermomechanical Measurements on Thermal Microactuators

Leslie M. Phinney, David S. Epp, Michael S. Baker, Justin R. Serrano, and Allen D. Gorby

Prepared by
Sandia National Laboratories
Albuquerque, New Mexico 87185 and Livermore, California 94550

Sandia is a multiprogram laboratory operated by Sandia Corporation,
a Lockheed Martin Company, for the United States Department of Energy's
National Nuclear Security Administration under Contract DE-AC04-94AL85000.

Approved for public release; further dissemination unlimited.

Issued by Sandia National Laboratories, operated for the United States Department of Energy by Sandia Corporation.

NOTICE: This report was prepared as an account of work sponsored by an agency of the United States Government. Neither the United States Government, nor any agency thereof, nor any of their employees, nor any of their contractors, subcontractors, or their employees, make any warranty, express or implied, or assume any legal liability or responsibility for the accuracy, completeness, or usefulness of any information, apparatus, product, or process disclosed, or represent that its use would not infringe privately owned rights. Reference herein to any specific commercial product, process, or service by trade name, trademark, manufacturer, or otherwise, does not necessarily constitute or imply its endorsement, recommendation, or favoring by the United States Government, any agency thereof, or any of their contractors or subcontractors. The views and opinions expressed herein do not necessarily state or reflect those of the United States Government, any agency thereof, or any of their contractors.

Printed in the United States of America. This report has been reproduced directly from the best available copy.

Available to DOE and DOE contractors from
U.S. Department of Energy
Office of Scientific and Technical Information
P.O. Box 62
Oak Ridge, TN 37831

Telephone: (865) 576-8401
Facsimile: (865) 576-5728
E-Mail: reports@adonis.osti.gov
Online ordering: http://www.osti.gov/bridge

Available to the public from
U.S. Department of Commerce
National Technical Information Service
5285 Port Royal Rd.
Springfield, VA 22161

Telephone: (800) 553-6847
Facsimile: (703) 605-6900
E-Mail: orders@ntis.fedworld.gov
Online order: http://www.ntis.gov/help/ordermethods.asp?loc=7-4-0#online

SAND2009-0521
Unlimited Release
Printed Month 2009

Thermomechanical Measurements on Thermal Microactuators

Leslie M. Phinney, David S. Epp, Michael S. Baker, Justin R. Serrano, and Allen D. Gorby
Sandia National Laboratories
P.O. Box 5800
Albuquerque, New Mexico 87185

Abstract

Due to the coupling of thermal and mechanical behaviors at small scales, a Campaign 6 project was created to investigate thermomechanical phenomena in microsystems. This report documents experimental measurements conducted under the auspices of this project. Since thermal and mechanical measurements for thermal microactuators were not available for a single microactuator design, a comprehensive suite of thermal and mechanical experimental data was taken and compiled for model validation purposes. Three thermal microactuator designs were selected and fabricated using the SUMMiT V^{TM} process at Sandia National Laboratories. Thermal and mechanical measurements for the bent-beam polycrystalline silicon thermal microactuators are reported, including displacement, overall actuator electrical resistance, force, temperature profiles along microactuator legs in standard laboratory air pressures and reduced pressures down to 50 mTorr, resonant frequency, out-of-plane displacement, and dynamic displacement response to applied voltages.

Acknowledgments

The authors gratefully acknowledge funding and support from the Campaign 6 program managed by T. Y. Chu. The authors appreciate the efforts Katie Francis during the design of the RS539 structures and Javier Gallegos in packaging parts for testing in the Linkam stage at low pressures. In addition, we thank Bruce Hansche for conducting the interferometric tests and David Luck for assistance with the displacement, resistance, and force measurements tests. The authors also appreciate the careful, technical reviews of this report by John Torczynski and Anton Sumali.

Contents

Figures

Tables

1. Introduction

Sandia microelectromechanical systems (MEMS) components are being designed and developed as future candidates for insertion into critical systems because they provide differentiating advantages due to their extremely small size, volume, mass, and power requirements. As the focus of MEMS design shifts from initial prototypes to system insertion, understanding the physical phenomena governing behavior for devices and materials at small scales becomes critical. Identification and characterization of critical phenomena enables improvements in modeling tools and supports validation efforts. In MEMS, thermal and mechanical phenomena are strongly coupled, motivating a Campaign 6 project to investigate thermomechanical phenomena in microsystems. The long-term goals of this project were to further understanding of thermomechanical phenomena, develop and improve diagnostic techniques to measure thermomechanical responses, enable predictive simulations of device performance, collect validation data, and provide input for design optimization for microsystems.

Thermal microactuators are enabling components in many of the envisioned Sandia National Laboratories MEMS designs. Advantages of MEMS thermal actuators include higher force generation, lower operating voltages, and less susceptibility to adhesion failures compared to electrostatic microactuators. Thermal microactuators do have higher power requirements than electrostatic microactuators, and their switching speeds are limited by the cooling time. Extensive work has been performed designing, fabricating, testing, and modeling thermal actuators.

Designs of electrically powered MEMS thermal actuators include actuators fabricated from a single material (Comtois et al., 1998; Que et al., 2001; Park et al., 2001) or bimorphs (Ataka et al., 1993). Thermal actuator designs using a single material are both symmetric, referred to as bent-beam or V-shaped, structures (Baker et al., 2004; Park et al., 2001) and asymmetric (Comtois et al., 1998), which have a hot arm and a cold arm. Asymmetric actuators are often referred to as flexure actuators. Modeling efforts have focused on bent-beam microactuators (Baker et al., 2004; Lott et al., 2002; Enikov et al., 2005; Wong and Phinney, 2007) and flexure actuators (Mankame and Ananthasuresh, 2001). Some studies examine both bent-beam and flexure actuators (Hickey et al., 2003; Oliver et al., 2003). The Wong and Phinney (2007) modeling effort employed the Calore code developed by Sandia National Laboratories (Calore, 2006; Calore, 2008).

A variety of mechanical and thermal measurements have been reported for thermal microactuators that can be used for model validation; however, a comprehensive set of measurements for a particular thermal microactuator design was not available. Since the thermal and mechanical measurements are obtained on varying microactuator designs, validating thermomechanical models is more challenging. This report compiles thermal and mechanical measurements for bent-beam polycrystalline silicon thermal microactuators, including displacement, overall actuator electrical resistance, force, temperature profiles along microactuator legs in standard laboratory air pressures and reduced pressures down to 50 mTorr, resonant frequency, out-of-plane displacement, and dynamic displacement response to applied voltages.

2. Thermal Microactuator Designs and Fabrication

Three thermal microactuators were investigated in this study and were fabricated using sacrificial surface micromachining techniques at Sandia National Laboratories. The thermal actuators are fabricated from polycrystalline silicon (polysilicon). Two thermal actuator designs are identical with regard to the actuator: one is the thermal microactuator and one has a force gauge attached to the thermal microactuator. The third microactuator design has the same actuator leg lengths; however, the gap beneath the actuator and the substrate is larger, and the beam thickness is slightly less. The thermal actuators were originally designed for the Compliant Thermo-Mechanical MEMS Actuators LDRD #52553 (Baker et al., 2004).

2.1 Fabrication

The surface micromachined thermal actuators used in this study were fabricated using the SUMMiT V™ (Sandia Ultra-planar Multilevel MEMS Technology) process (Sniegowski and de Boer, 2000; SUMMiT V, 2008). The SUMMiT V process uses four structural polysilicon layers with a fifth layer as a ground plane. These layers are separated by sacrificial oxide layers that are etched away during the final release step. The two topmost structural layers, Poly3 and Poly4, are nominally 2.25 μm in thickness, while the bottom two, Poly1 and Poly2, are nominally 1.0 μm and 1.5 μm in thickness, respectively. The ground plane, Poly0, is 300 nm in thickness and lies above an 800 nm layer of silicon nitride and a 630 nm layer of SiO_2. The sacrificial oxide layers between the structural layers are each around 2.0 μm thick (Sniegowski and de Boer, 2000; SUMMiT V, 2008).

2.2 Thermal Actuator Designs

Figure 1 contains a schematic of a bent-beam thermal microactuator with two actuator legs and a cross-sectional area of an actuator leg with the width and thickness dimensions labeled. The SUMMiT V processing constraints on the sacrificial oxide cut between two polysilicon layers result in an I-beam shape for the thermal actuator legs (SUMMiT V, 2008). The three actuators investigated are bent-beam thermal microactuators with two actuator legs.

The first thermal actuator design has the actuator legs fabricated from three laminated structural polysilicon layers: Poly1, Poly2, and Poly3 (Figure 2). This actuator design is referred to as the P123 actuator throughout this report. The second thermal actuator design has the same thermal actuator as the first design with a force gauge attached to the actuator shuttle (Figure 3) and is referred to as the P123F actuator. The force gauge consists of a linear bi-fold spring attached to the shuttle of the actuator using the Poly3 layer. The third thermal actuator design is very similar to the first design, except the microactuator legs are made from a laminate of the top two structural polysilicon layers, Poly3 and Poly4 (Figure 4). This actuator design is referred to as the P34 actuator throughout this report. Table 1 summarizes the geometries of the three thermal microactuators examined with nominal dimensions specified according to the SUMMiT V Design Manual (SUMMiT V, 2008). The shuttle that connects beams at the center is 10 μm wide, 100 μm long and its thickness is the sum of t_1, t_2, and t_3. The P123, P123F, and P34

actuators were fabricated on reticle set 415 (RS415). The P123 thermal actuators for temperature measurements in varying pressures are an identical design to the P123 microactuators on RS415 and were fabricated during a later fabrication run, reticle set 539 (RS539).

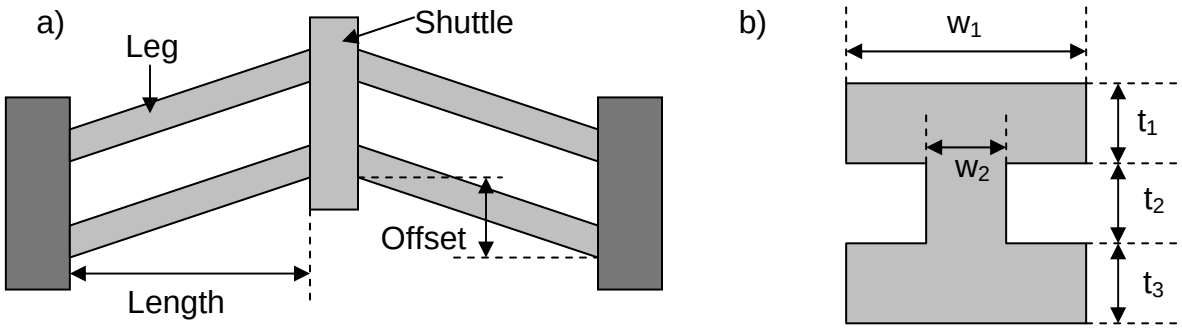

Figure 1: Schematics of a) bent-beam thermal actuator and b) actuator leg cross section

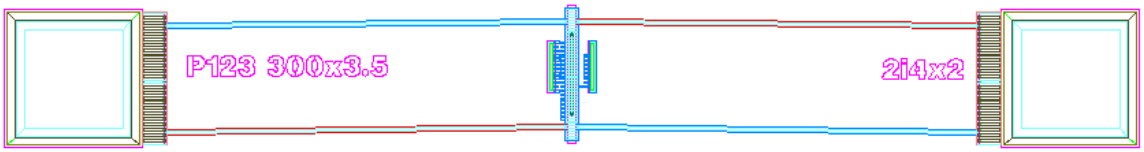

Figure 2: P123 thermal microactuator

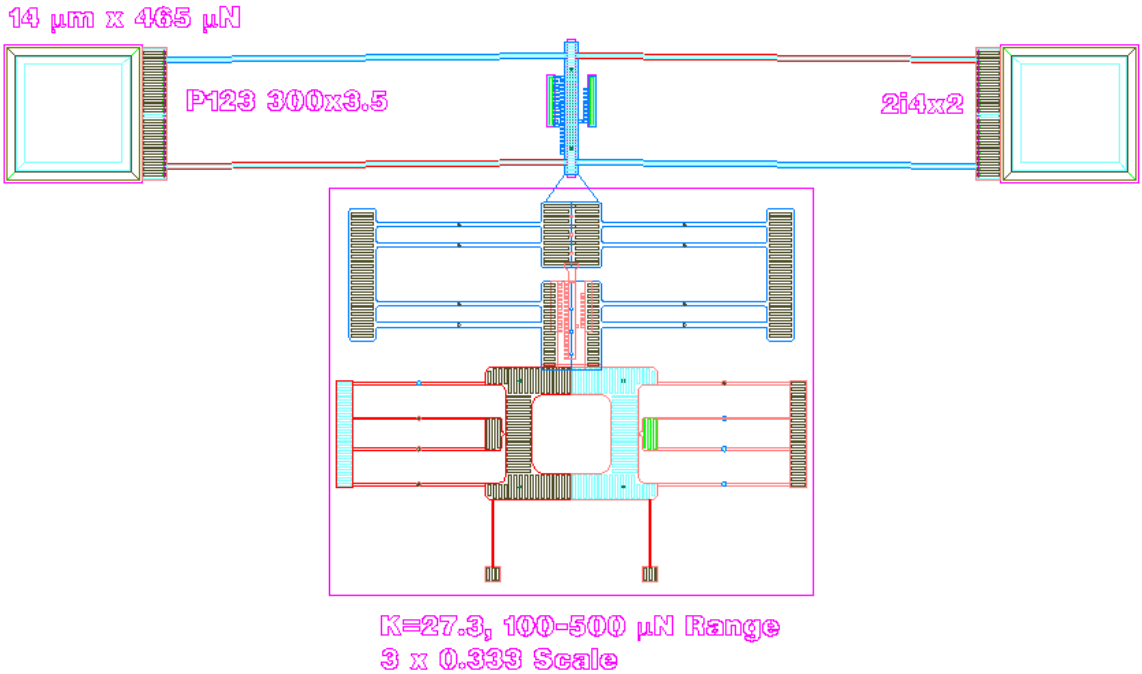

Figure 3: P123F microactuator with an attached force gauge

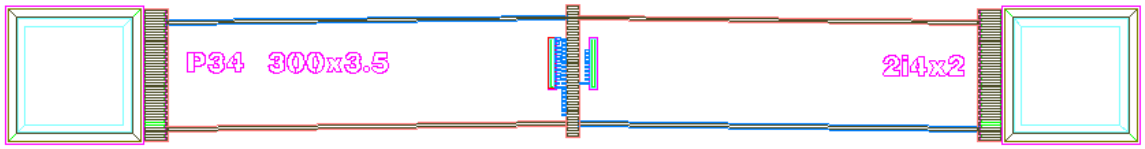

Figure 4: P34 thermal microactuator

Table 1: Summary of microactuator geometries

Actuator	Gap to Substrate [μm]	Length [μm]	Offset [μm]	w_1 [μm]	w_2 [μm	t_1 [μm]	t_2 [μm]	t_3 [μm]	Force Gauge
P123	2.0	300	3.5	4.0	2.0	2.5	2.0	2.25	No
P123F	2.0	300	3.5	4.0	2.0	2.5	2.0	2.25	Yes
P34	6.5	300	3.5	4.0	2.0	2.25	2.0	2.25	No

3. Displacement, Resistance, and Force Measurements

During operation of an electrically powered thermal microactuator, a current is applied to create a displacement or force output. Displacement and total actuator resistance measurements as a function of input current are standard metrics of thermal microactuator performance and are used for design comparison and model validation. The output force as a function of position is an additional metric for thermal actuator mechanical behavior.

3.1 Methods

The measurements in this section were performed according to methods described Baker et al. (2004). Displacement and total electrical resistance results were measured on a probe station using a National Instruments Vision software package that performs sub-pixel image tracking. A displacement measurement error of ±0.25 μm was achieved by using 200X magnification. Force measurements were made using the P123F actuator design, in which a linear bi-fold spring is attached to the movable shuttle of the actuator. Force is applied manually to the actuator with a probe tip through the pull-ring attached to the spring. The displacement for a given force is determined from the vernier scale with ±1/6 μm resolution. The applied force is determined from the measured displacements and calculated spring stiffness. This method of force measurement was used due to the lack of other methods viable for force measurements at this scale.

3.2 Displacement Results

Figures 5 and 6 show the displacement versus applied current for the P123 and P34 thermal actuators, respectively. The positive displacement from the designed zero location at zero current is due to compressive residual stress resulting from fabrication processes. The model results shown on the figures are for the thermomechanical model presented by Baker et al. (2004). When a bias is specified after "Model" in the legend, the bias represents an edge bias which is subtracted from each side of thermal actuator leg nominal width. If a bias is not specified, the nominal width, 4.0 μm, is used in the model calculations.

As the current is increased, the displacement versus current data exhibit an inflection point and roll-off in the curve. This is attributed to the maximum temperature in the thermal actuator legs becoming hot enough, above 550°C, that the polysilicon is softened or even melts (Baker et al., 2004). The thermal actuator legs have been observed to glow red under these conditions. The displacement for a given current is larger for the P34 actuator compared to the P123 actuator since the temperatures for a given current are larger. The higher temperatures in the P34 microactuator at a given current are due to a smaller total thickness, 6.5 μm versus 6.75 μm, and to the reduced heat transfer from the microactuator to the substrate through the intermediate gas due to the larger gap underneath the P34 thermal microactuator in comparison to the P123 thermal microactuator.

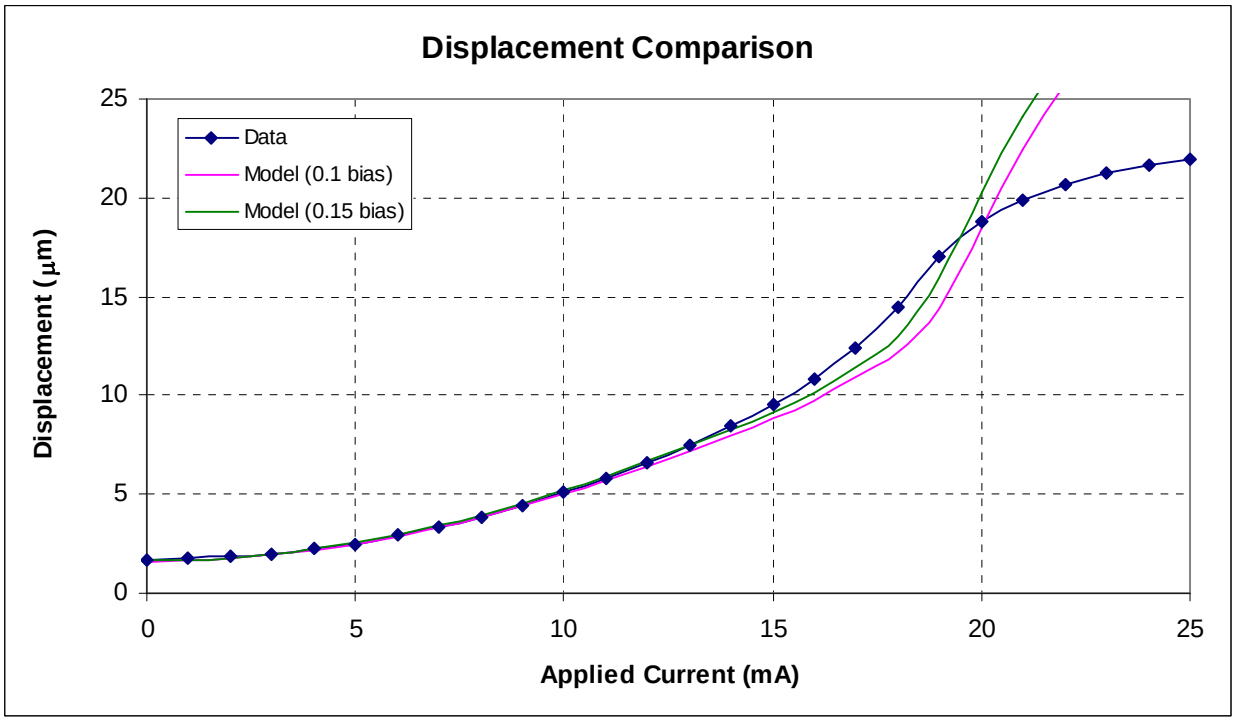

Figure 5: Displacement versus current for the P123 thermal actuator

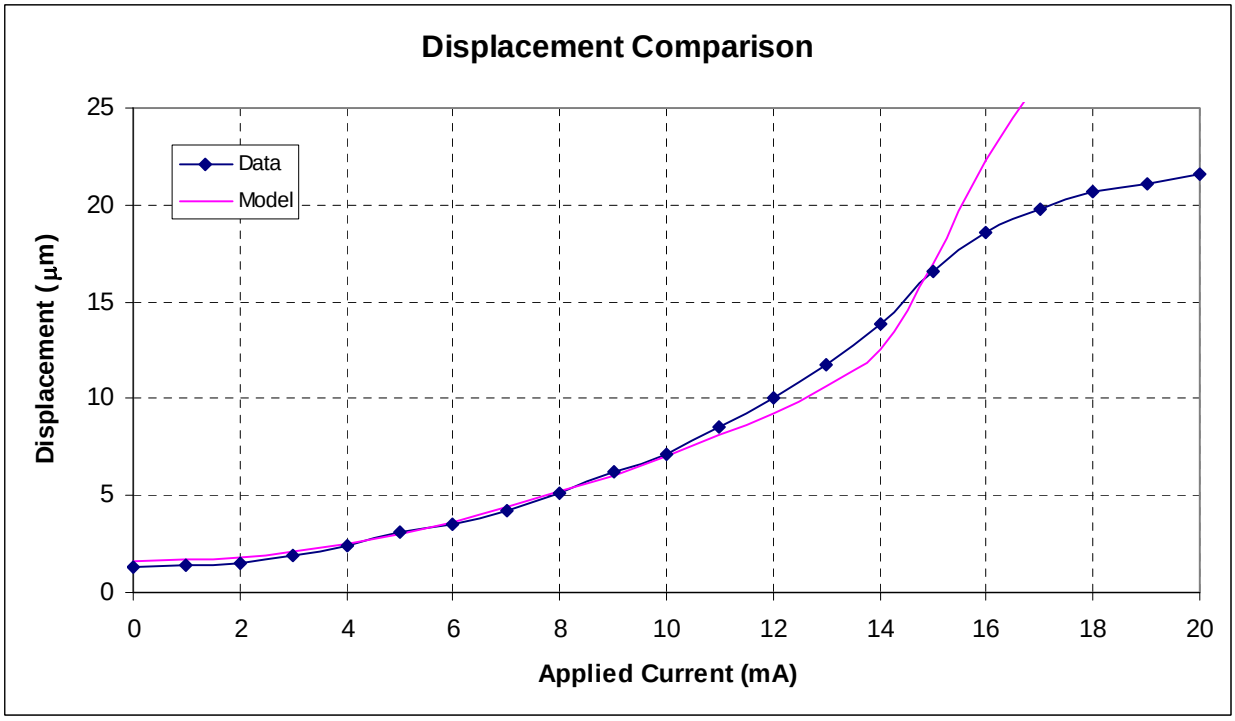

Figure 6: Displacement versus current for the P34 thermal actuator

3.3 Resistance Results

Figures 7 and 8 show the total electrical resistance for the actuators versus applied current for the P123 and P34 thermal actuators, respectively. The resistance curves exhibit an inflection point, followed by a maximum, and then a decrease in resistance as the current is increased. The resistance of the P34 thermal actuators is higher than those of the P123 actuators due to the actuator legs and shuttle being 0.25 μm thinner than the P123 actuators. Additionally, the P34 is heated to a higher temperature for the same applied current resulting in the electrical resistance increasing at a greater rate in the P34 thermal actuators than in the P123 thermal actuators.

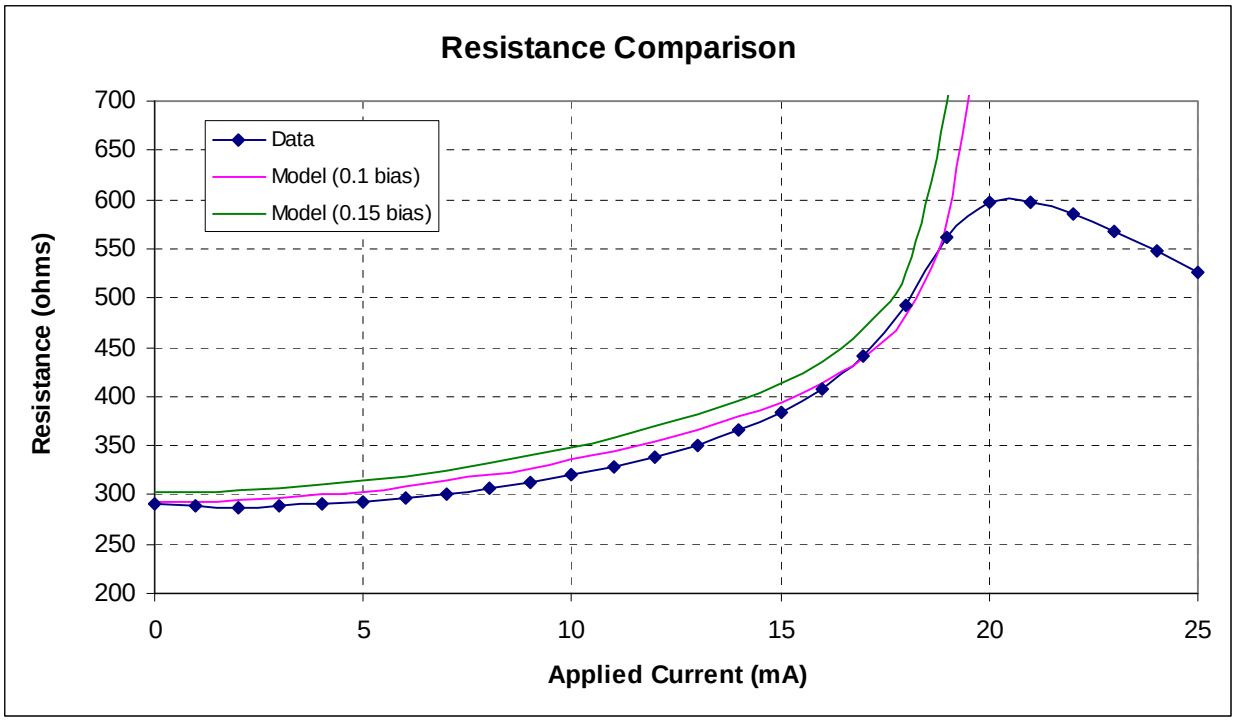

Figure 7: Resistance versus current for the P123 thermal actuator

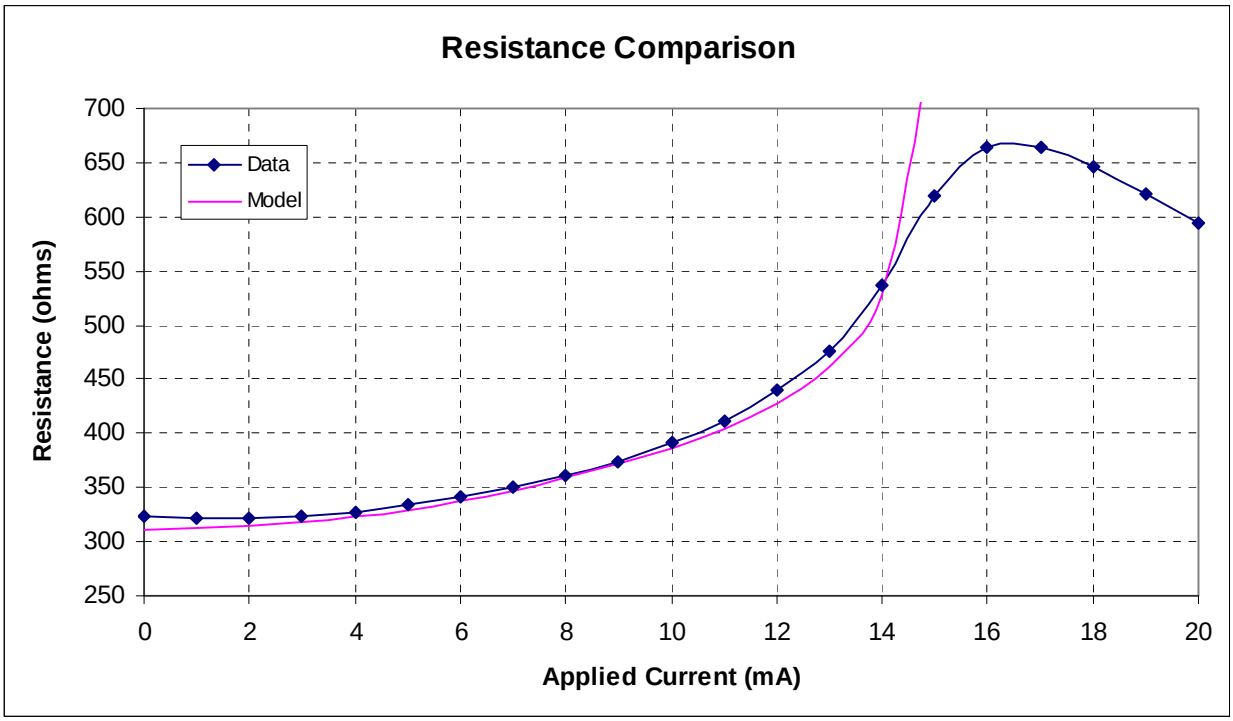

Figure 8: Resistance versus current for the P34 thermal actuator

3.4 Force Results

Figure 9 shows the force for P123F thermal actuator versus displacement when actuated at a constant current and voltage, 15 mA and 6.1V (Baker et al., 2004). For this test, the thermal actuator was held at a constant applied current and allowed to displace to its maximum unloaded position, which corresponds to the point on the graph where the curve intersects with the X-axis. Then using a probe tip, the force gauge was pulled away from the actuator, stretching the folded-beam spring in series between the probe tip and the actuator and applying a force to the thermal actuator center shuttle. The spring elongation was used to calculate the applied force and was recorded with the actuator displacement. As the actuator is pulled back, the force increased to a maximum of 205 mN at ~6.75 μm. When pulled beyond this, the force begins to decrease due to buckling of the actuator legs. It is important to understand that this force curve represents the available output force of this single actuator design at this single applied power level. To fully characterize the force output of an actuator design, a force curve would need to be measured at several different power levels. This family of curves would then map out the full force versus displacement behavior. The error bars shown for each force level were determined based on an uncertainty analysis performed on the spring design, taking into account the uncertainty in beam width, length, thickness and Young's Modulus, as well as the measurement uncertainty in the spring elongation.

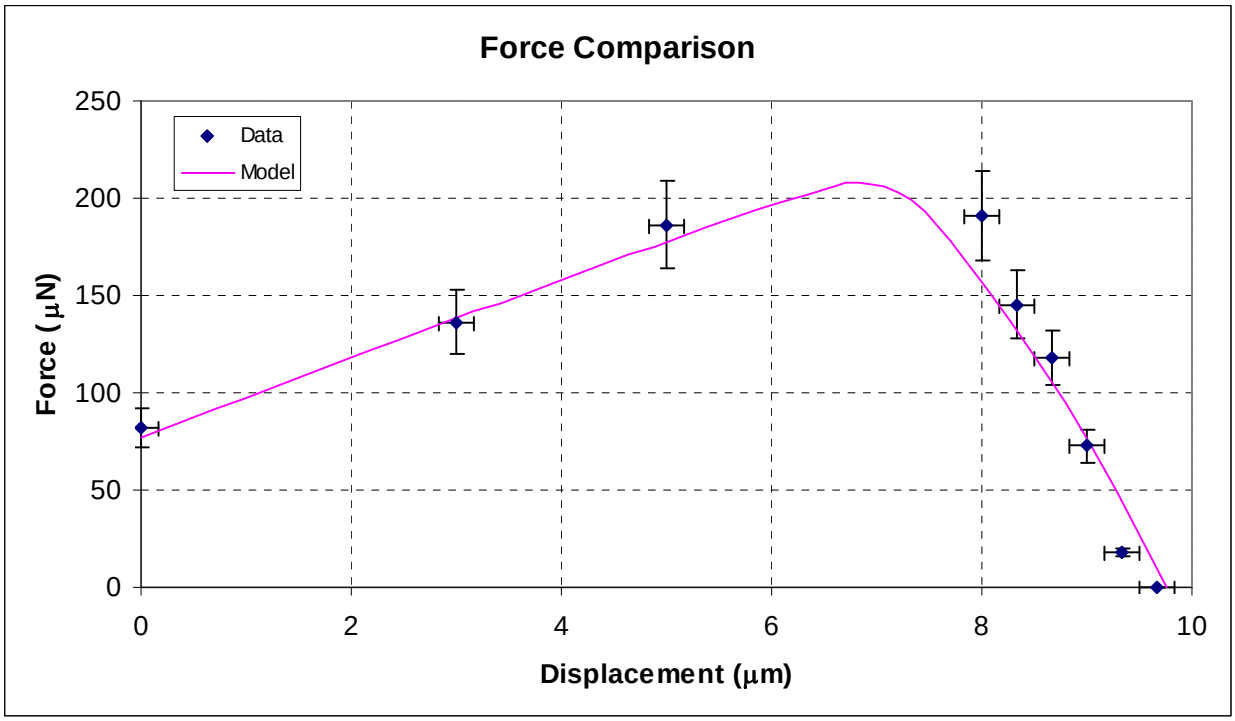

Figure 9: Force versus position of the actuator at 15 mA for the P123F thermal actuator

4. Temperature Measurements

Due to the challenges associated with obtaining spatially resolved temperature measurements on MEMS thermal actuators, thermal microactuator models have often been validated primarily from displacement and electrical measurements. Thermal actuator performance depends on the temperatures of the microactuator legs. Experimentally measured temperatures are invaluable for understanding thermal microactuator performance, model validation, and design optimization. Raman thermometry techniques were used to measure temperatures on the bent-beam thermal microactuators. Since the heat transport from a thermal microactuator depends on the atmospheric pressure due to a portion of the heat transfer from the microactuator to the substrate being through the underlying gas, temperature measurements were made at reduced pressures as well as in standard laboratory air.

4.1 Methods

Raman thermometry has been used to measure temperature profiles along the actuator legs of bent-beam and flexure thermal microactuators (Kearney et al., 2006a and 2006b; Serrano et al., 2006). The 1.2 μm in-plane resolution of the Raman probe is capable of resolving widths of 2 μm to 4 μm for thermal microactuator legs. A detailed uncertainty analysis reveals that the reported Raman-measured temperatures are reliable to within ±10 to 11 K (Kearney et al., 2006a). These experimental results show that high-quality, reliable temperature measurements can be obtained. The temperature profiles reported in this manuscript were taken using the same techniques as those reported by Kearney et al. (2006a, 2006b) on the surface micromachined actuators described in Section 2. In addition, some measurements were performed at nitrogen pressures varying from 0.05 Torr to 630 Torr using the methods described in Torczynski et al. (2008). Temperature measurements are made along one leg of the thermal microactuators starting from an anchor and ending at the center shuttle since the design and performance are symmetric.

The RS415 dice with the P123, P123F, and P34 thermal microactuators were die attached and wire bonded in 24-pin Dual-in-Line Packages (DIP) that were inserted into a zero insertion force (ZIF) socket for the testing in laboratory air. The devices were powered with a Keithley 2400 Source Meter with a single lead on each anchor of the thermal microactuator. For the reduced pressure measurements inside a Linkam thermal stage for which the pressure was controllable, a RS539 SUMMiT die with a P123 microactuator was packaged on a printed circuit board (PCB) to which wire leads were soldered. Each bond pad on the beam structure is wire-bonded to two separate connections on the PCB to allow for four-point sensing of the voltage. Quick-disconnect connectors were used inside the Linkam thermal stage to allow for easy exchange of parts. The PCB was placed in the center of a quartz crucible inside the stage and held in place with vacuum-compatible carbon tape. The heating ability of the stage was used to heat the sample to a temperature of 300-310 K to ensure a consistent substrate temperature for the measurements. The devices were powered with a Keithley 2400 Source Meter in a four-point sensing configuration, where the current is sourced through the outside connections and the voltage is measured across the inner ones.

4.2 Temperature Measurement Results in Laboratory Air

Raman thermometry was used to measure temperatures along the lower left leg of P123 (four cases) and P123F (one case) thermal microactuators (Figure 10). P123 microactuators on two packages, P5 and P6, were tested at two currents, 12 mA and 15 mA. The agreement between the temperature profiles for the P5 and P6 microactuators is within the experimental uncertainty of ±10 to 11°C. Thus, the observed device-to-device variation is within the measurement uncertainty. As the current is increased from 12 mA to 15 mA, the maximum temperature increases significantly from 210°C to 377°C. The maximum temperatures along the microactuator legs occur at about two-thirds of the distance from the anchor to the shuttle. Since these tests were conducted at laboratory air pressures, heat transport from the shuttle to the cooler underlying substrate results in the shuttle acting as a heat sink. The temperature profile along a P123F microactuator leg (P5 F) at 12 mA decreases even more at the shuttle than for P123 microactuators tested at 12 mA due to the connection to the force gauge providing another pathway for energy transport away from the shuttle.

Figure 11 graphs the temperature profiles along the lower left leg of P34 thermal microactuators in packages P5 and P6. Measurements were collected at 10 mA and 12 mA, and the measurements on the microactuators from the two packages exhibit good agreement. The maximum temperature for a P34 microactuator is higher than for a P123 microactuator operated at the same current because of the larger gap under the P34 microactuators inhibiting the transfer of energy from the microactuator to the cooler underlying substrate and the smaller thickness of the P34 microactuator legs, 6.5 μm versus 6.75 μm. Table 2 summarizes the average displacements, currents, voltages, and maximum temperatures for the P123 and P34 thermal microactuators.

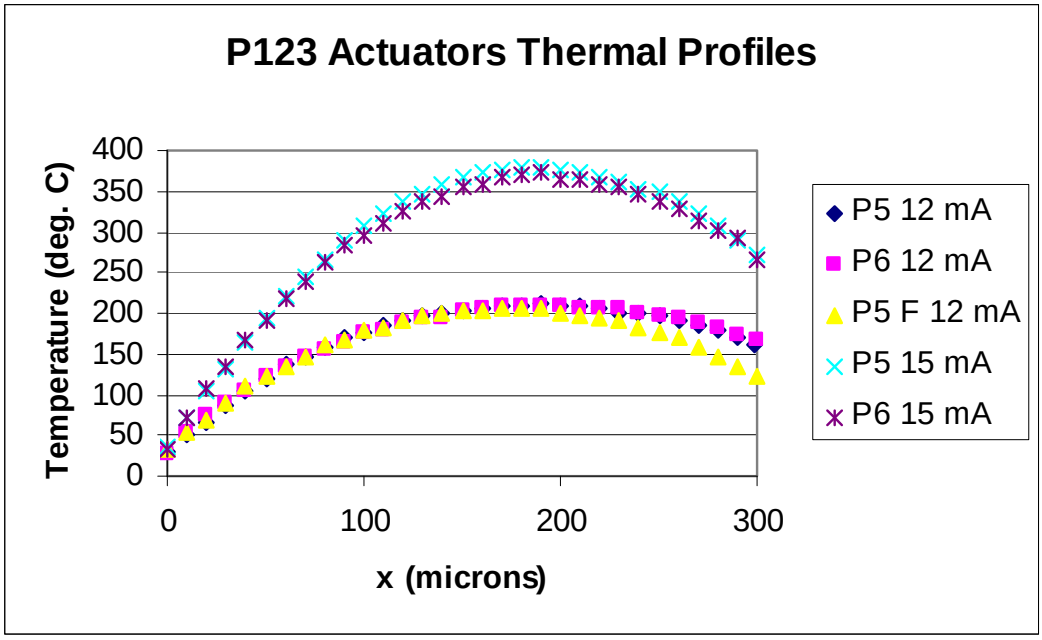

Figure 10: Temperature profiles for the lower left leg of the P123 and P123F thermal actuators

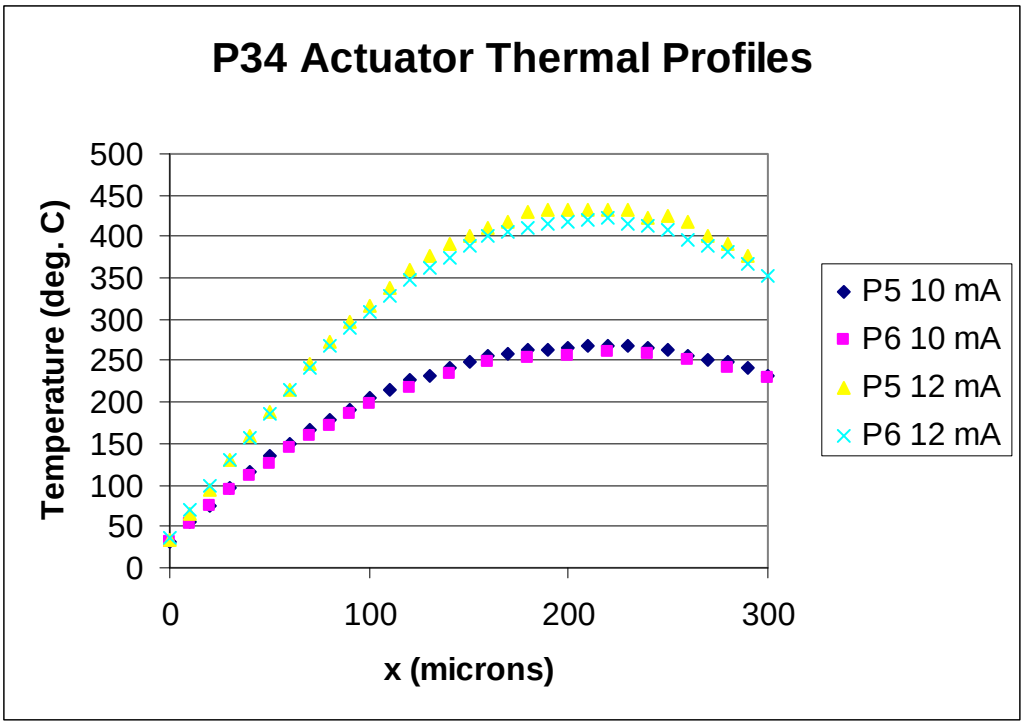

Figure 11: Temperature profiles for the lower left leg of the P34 thermal actuator

Table 2: Average actuator displacements, electrical measurements, and maximum temperatures at laboratory air pressure

Actuator	Current [mA]	Voltage [V]	Displacement [μm]	Maximum Temperature [°C]
P123	12	3.89	6.67	210
P123	15	5.58	9.61	377
P34	10	3.87	6.54	265
P34	12	5.38	9.66	428

4.3 Temperature Measurement Results at Varying Pressures

Microsystems devices are often packaged at pressures lower than atmospheric, which dramatically affects the thermal performance of the parts since energy transfer to the environment is substantially reduced as the pressure is reduced. Thus, temperature measurements of thermal microactuators in varying pressures are crucial to optimizing device and package design as well as model validation.

Raman thermometry was used to measure the temperature profiles for a P123 microactuator leg at pressures ranging from 0.05 Torr to 630 Torr (Figure 12). In order to maintain similar maximum temperatures in the P123 microactuator as the pressure reduced, the power applied to the microactuator was reduced as the pressure was decreased. The P123 microactuator power

versus pressure is plotted in Figure 13. At pressures below about 5 Torr, the rate of decrease in the power to maintain the maximum temperature is less than at higher pressures (Figure 13).

As seen in Figure 12, the location of the maximum temperature along the microactuator leg moves from around two-thirds of the distance from the anchor to the shuttle to the shuttle as the pressure is reduced. Heat transfer through the underlying gas from the microactuator to the cooler underlying substrate is significantly reduced as the pressure is decreased. At lower pressures, sufficient energy is not transferred from the shuttle to the substrate to allow the shuttle to maintain a lower temperature and act as a heat sink. The location of maximum temperature therefore moves from being on the microactuator legs at high pressures to being at the shuttle at the lower pressures. Table 3 summarizes the operating conditions used (pressure and current) as well as the voltage, resistance, power, displacement, magnitude and location of the temperature maximum, and the average temperature at the various pressures. It is important to note that, although the location and magnitude of the temperature maximum varies with pressure the length-averaged temperature, $\overline{T} = \frac{1}{L}\int T(x)dx$, remains fairly constant for all pressures, thus yielding the similar resistance and displacement values observed.

Figure 14 presents the temperature versus position on the P123 microactuator leg for the seven pressures at which data was collected. The data is the same as that in Figure 12 and is replotted in individual graphs to facilitate obtaining a particular data point.

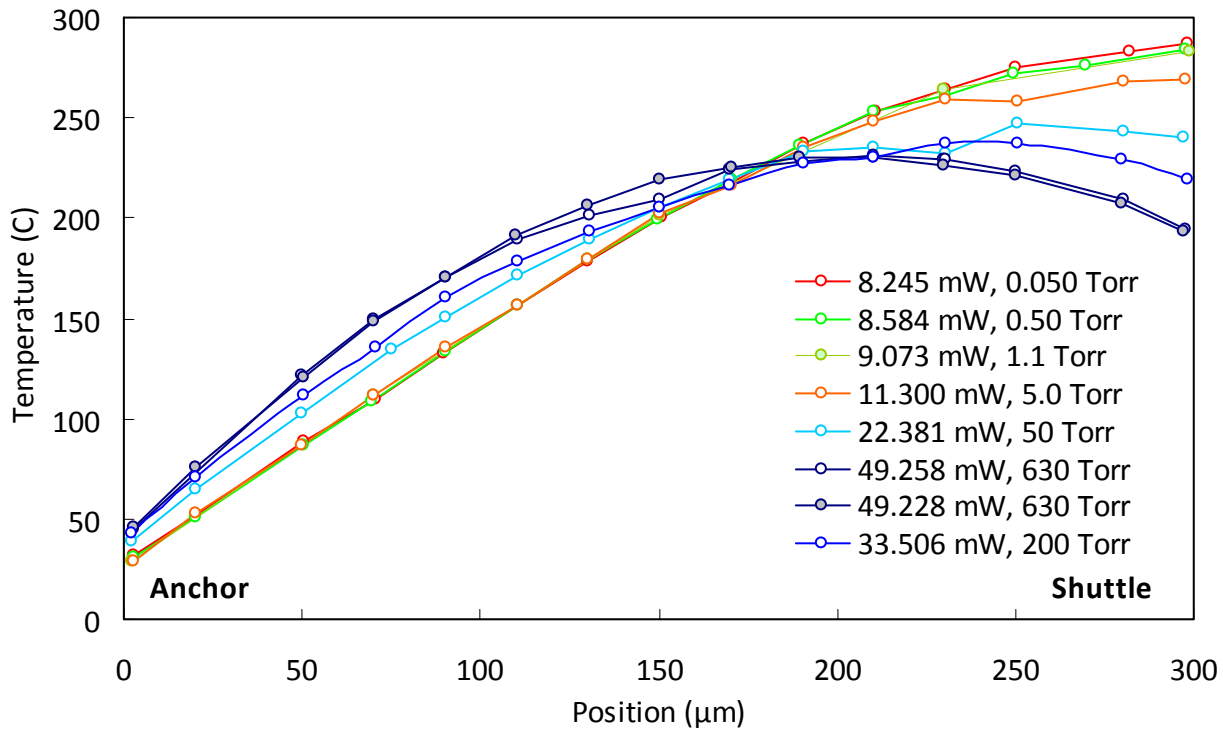

Figure 12: Temperature profiles for a P123 microactuator leg at 0.05 to 630 Torr

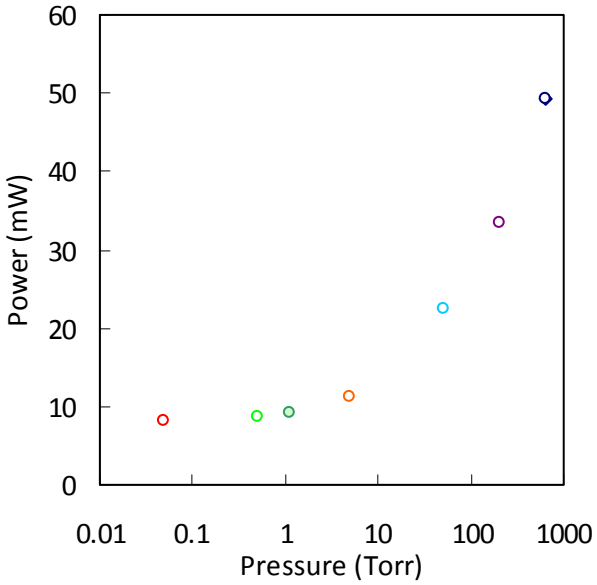

Figure 13: Operating power for P123 thermal microactuator as a function of pressure for a constant actuator resistance

Table 3: Actuator displacements, electrical measurements, location and magnitude of the temperature maxima, and average temperature under various nitrogen pressures

Pressure [Torr]	Current [mA]	Voltage [V]	Resistance [Ω]	Power [mW]	Displacement [μm]	Maximum Temperature [°C]	Location of Maximum [μm]	Average Temperature [°C]
0.050	4.910	1.67925	342.006	8.245	5.01	287	298.3	186
0.50	5.010	1.7133	341.976	8.584	5.01	284	297.9	185
1.1	5.150	1.76167	342.072	9.073	5.01	283	298.6	184
5.0	5.750	1.9653	341.791	11.300	5.01	269	297.6	182
50.0	8.090	2.7665	341.965	22.381	5.01	248	250.4	182
200	9.900	3.3844	341.859	33.506	5.01	238	230.4	182
630	12.000	4.1048	342.067	49.258	5.01	231	210.2	183
630	12.000	4.1023	341.858	49.228	5.01	230	210.2	184

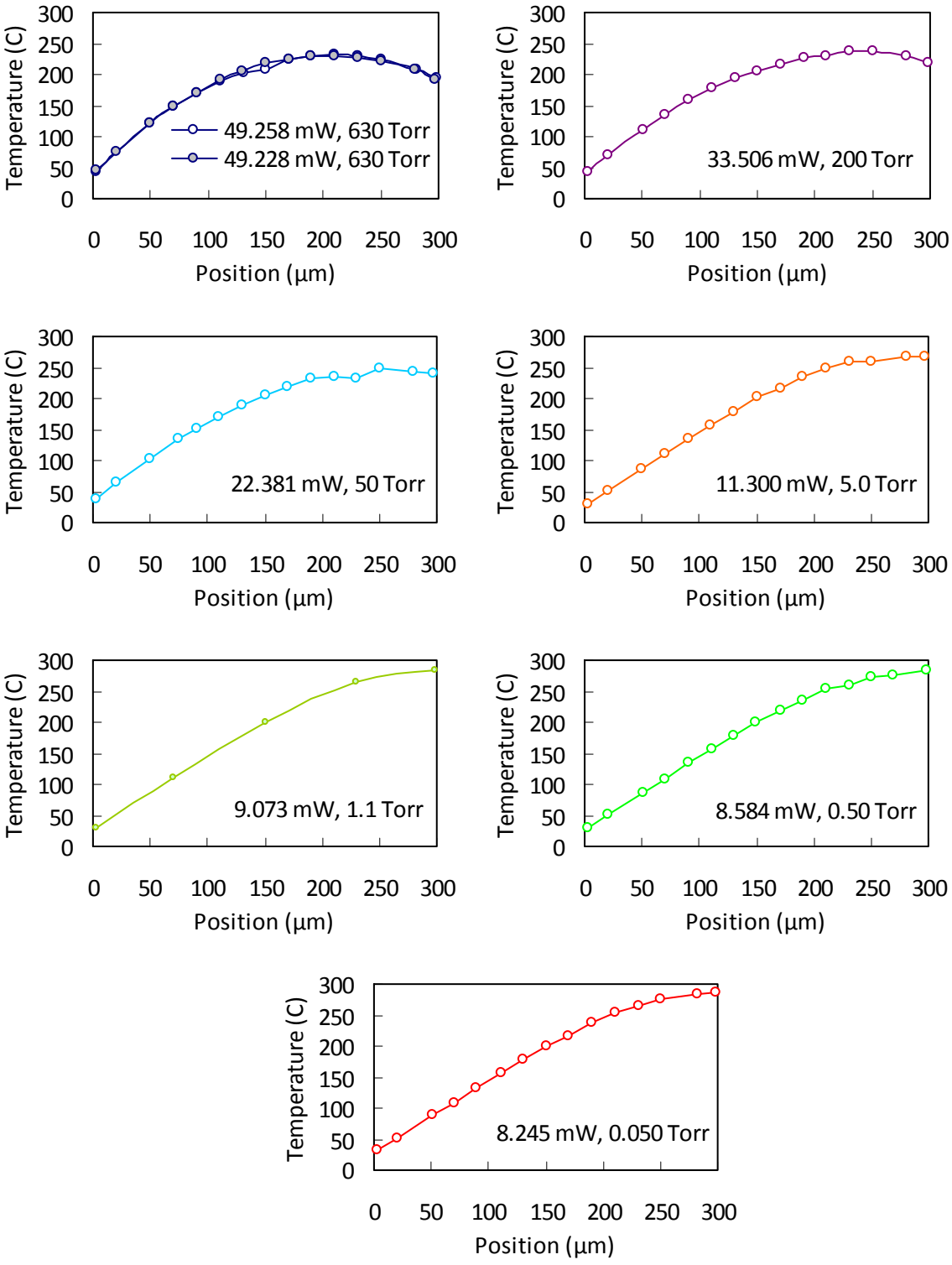

Figure 14: Temperature profiles for a P123 microactuator leg at 0.05 to 630 Torr

5. Resonant Frequency Measurements

One method for validating structural dynamics models is to make comparisons of the predicted linear resonant frequencies with those measured on real parts. To facilitate such a comparison, the first resonant frequencies of three thermal actuator parts were measured, and the results are presented here. High-speed imaging of a step relaxation event was used to determine these resonant frequencies.

5.1 Methods

A probe tip was used to push the thermal actuators away from equilibrium with no changes in environmental temperature or any electrical inputs. The probe tip was then moved in such a way that the force generated by the probe would decrease in a step function, allowing the thermal actuator to ring down to the equilibrium position. A high-speed camera was used to capture this event, and the images generated were analyzed to determine the resonant frequencies. The limitation with this method is the limited frame rate of the camera. The highest speed possible, while retaining enough features on the image to make it useful, was 148148 Hz (6.75 μs frame rate). In every case tested, the resonant frequencies were above half the sample rate, thus generating an aliased response. The aliased data was unwrapped to get the correct resonant frequencies. The results of this operation were verified by recollecting data at 133333 Hz (7.5 μs frame rate) and again unwrapping the data.

Unfortunately, only the P34 and the P123F actuators could be measured with this technique. The response frequency of the P123 actuators was too high to be captured with the shutter speeds available on the camera. While the shutter speeds available are significantly faster than the available sample rates, they were still too slow to prevent blurring of the images.

5.2 Results

The movies collected with the high speed camera were truncated so that they included a few frames prior to the release of the probe tip force and the complete ring down of the actuator. Complete ring-down in this case was when the actuator oscillation decayed to zero visually. These movies were then analyzed using an NI Labview function for feature tracking to generate a time history of the actuator shuttle position. Figure 15 shows the resulting displacement time histories and the FFT results for the P34 actuator tested on part #5. The two peaks on the FFT results correspond to 28385 Hz for the 133333 Hz sample rate and 43113 for the 148148 Hz sample rate. Unwrapping each of these once gives the final result 104991 Hz in both cases. Table 4 and Table 5 show the results from all the cases measured. The error reported is the frequency spacing on the FFT operation (essentially the readability). There is very good agreement for both actuators (P123F and P34) that could be measured, indicated by the standard deviations that are about 1% of the reported frequencies.

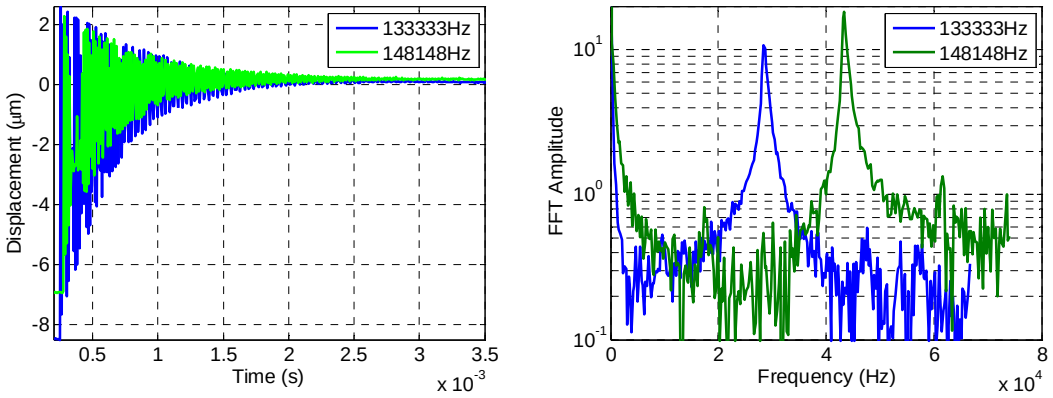

Figure 15: Time histories and FFT results for the P34 actuator on part #5. Legend indicates sample rate.

Table 4: Measured resonant frequency results for the P123F actuators

Part #	Measured Resonant Frequency (Hz)
3	95804 ± 289
4	94328 ± 289
5	94907 ± 289
Mean	95013
Std Dev	744

Table 5: Measured resonant frequency results for the P34 actuators

Part #	Measured Resonant Frequency (Hz)
3	106495 ± 289
4	105121 ± 289
5	104991 ± 289
Mean	105536
Std Dev	834

6. Out-of-Plane Displacement Measurements

There is some evidence available indicating that the thermal actuators do not travel parallel to the substrate when they are actuated. Wear debris has been observed coming from under actuators that have been operated for long periods of time, and trenches were found under the shuttles when failure analysis was performed. There are no trends that have been found to predict when this type of out-of-plane motion will occur with actuation. The measurements here were an attempt to find any trends by measuring the shuttle out-of-plane displacement rather than looking at the secondary indicator of the wear debris.

6.1 Methods

The "Sinclair" microscope is an adjustable, two-leg, balanced interferometric microscope (Sinclair et al., 2005). It is designed to provide interferometrically balanced legs for 5X and 10X long working distance Mitutoyo microscope objectives. We adapted our Sinclair microscope for out-of-plane motion measurement of the thermal actuator shuttles using optics we had on hand. The size of the shuttles required a 50X microscope objective, which the adjustable reference arm of the microscope could not balance properly. This provided an interferogram with some inherent lack of fringe uniformity, so the static fringe patterns cannot be interpreted as an indication of flatness or curvature of the shuttles. In order to obtain sufficient brightness for high-speed imaging, a 200 mW diode-pumped, frequency-doubled YAG laser (Coherent DPSS series) was substituted for the incoherent LED source in the original microscope. The laser was fiber coupled, with the beam injected at a similar location to the LED in the original design. Use of coherent light eliminated any concern for strict path length matching of the two interferometer arms.

The interferometer was adjusted to provide a fringe pattern which had five to ten fringes perpendicular to the long axis of the shuttle. Typically the fringes were approximately uniform in frequency. As mentioned, it was not clear whether any nonuniformity in fringe spacing was due to curvature of the actuator or to aberrations of the reference wavefront. The part was actuated with a 200 Hz square wave, and 256 by 64 pixel images of the interferogram were recorded at 100000 frames per second with a Vision Research Phantom 7 camera. Each image was averaged along the fringe direction (perpendicular to the long axis of the shuttle) for noise reduction, and the resulting one-dimensional fringe data were plotted as a function of time, creating a "streak camera" fringe plot. Out-of-plane motion was calculated by selecting a bright or dark fringe peak before the motion and visually counting the number of fringes that crossed this reference location during the motion. Each fringe represents an out-of-plane motion of $\lambda/2 = 0.266$ μm. Fractional fringe positions were estimated visually between local fringe maxima or minima, resulting in an accuracy of about ¼ fringe, or about 0.07 μm. The direction of the motion was determined by tilting the part in a known way so that fringe motion to the left (lower "position" coordinate) indicated upward motion (away from the base plane).

6.2 Results

A movie of the interferometric image was collected at 100 kHz. This movie was a series of interferograms like the one in Figure 16. The interference pattern is obscured significantly by the light and dark pattern on the shuttle from the manufacturing process. To eliminate that interference, a series of averaging and filtering steps was used. First, the data in the interferogram were averaged over the width of the shuttle for each frame in the movie collected. The resulting plot of average shuttle interferogram versus time is shown in Figure 17 along with a filtered version. The filtering process used was specifically designed to eliminate the shuttle pattern but leave the interference pattern. This was possible because the microscope was tuned to give an interference pattern on the shuttle that had a significantly different spatial frequency than the shuttle pattern. Once the filtered average shuttle interferogram was generated, fringes were counted along three lines (shown in red in Figure 17).

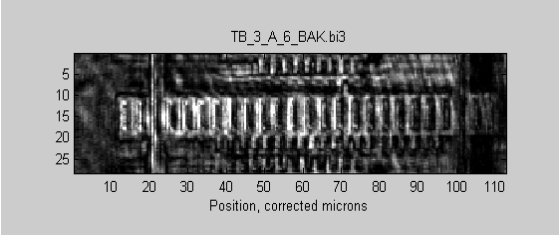

Figure 16: One frame of the interferogram movie for one of the parts tested.

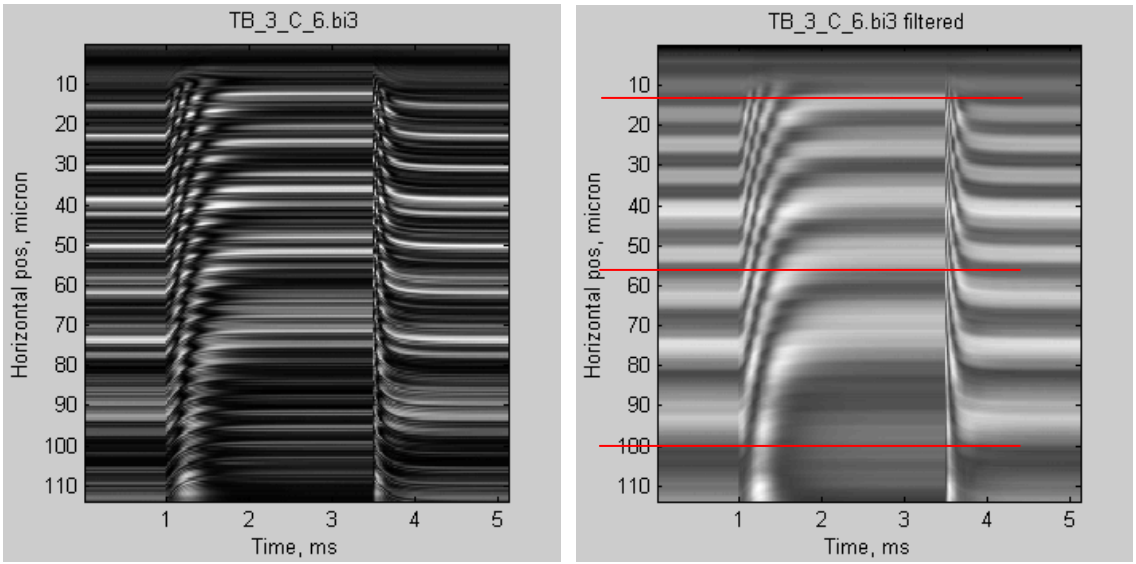

Figure 17: Average shuttle interferogram over time with and without smoothing filter. Lines in red show the measurement locations used.

The data collected directly from the interferograms yield the stationary vertical translation of a point on the shuttle plane close to each end. These points do not move with the shuttle. These two points, along with the measured shuttle translation in the actuation direction, were then used to calculate the translation and rotation of the shuttle. Table 6 through Table 8 show the calculated translation and rotation of the shuttle during actuation for two actuation voltages.

Positive translation corresponds to motion away from the substrate. Positive rotation indicates that the forward portion of the shuttle during actuation is moving up. The errors reported for the results are not uniform because the reported values are calculated from measurements. The propagation of the errors through the calculation produces an error value that is dependent on the measured values themselves as well as their errors.

Some of the parts did exhibit large rotation and/or translation, so the phenomenon is certainly occurring. The results do not really show much consistency, though, so it is difficult to draw significant conclusions.

Table 6: P123 out-of-plane response during actuation at the center of gravity (CG) of the shuttle

	4 V Excitation			5.7 V Excitation	
Part #	CG Out of Plane Translation (μm)	CG Rotation (degrees)	Part #	CG Out of Plane Translation (μm)	CG Rotation (degrees)
3	0 ± 0.024	0 ± 0.033	3	0.040 ± 0.024	0.048 ± 0.034
4	0 ± 0.024	0 ± 0.034	4	0.024 ± 0.024	-0.070 ± 0.050
7	-0.067 ± 0.024	0 ± 0.034	7	-0.133 ± 0.024	0 ± 0.037
8	-0.067 ± 0.024	0 ± 0.034	8	-0.133 ± 0.024	0 ± 0.034

Table 7: P123F out of plane response during actuation at the center of gravity (CG) of the shuttle

	4 V Excitation			5.7 V Excitation	
Part #	CG Out of Plane Translation (μm)	CG Rotation (degrees)	Part #	CG Out of Plane Translation (μm)	CG Rotation (degrees)
3	0.163 ± 0.024	-0.050 ± 0.035	3	0.671 ± 0.024	-0.537 ± 0.038
4	0.157 ± 0.024	-0.145 ± 0.034	4	0.660 ± 0.024	-0.570 ± 0.034
7	-0.043 ± 0.024	-0.157 ± 0.037	7	-0.012 ± 0.024	-0.227 ± 0.036
8	-0.006 ± 0.024	-0.102 ± 0.036	8	-0.031 ± 0.024	-0.309 ± 0.036

Table 8: P34 out of plane response during actuation at the center of gravity (CG) of the shuttle

	3.85 V Excitation			5.25 V Excitation	
Part #	CG Out of Plane Translation (μm)	CG Rotation (degrees)	Part #	CG Out of Plane Translation (μm)	CG Rotation (degrees)
3	-0.360 ± 0.024	0.055 ± 0.039	3	-0.532 ± 0.024	0 ± 0.036
4	-0.399 ± 0.024	0 ± 0.036	4	-0.599 ± 0.024	0 ± 0.033
7	-0.239 ± 0.024	-0.055 ± 0.039	7	-0.333 ± 0.024	0 ± 0.040
8	-0.067 ± 0.024	0 ± 0.034	8	-0.133 ± 0.024	0 ± 0.035

7. Dynamic Displacement Response to Voltage

The dynamic displacement response of the thermal actuator to a voltage input is an important characteristic that was not captured in the static deflection versus voltage plots presented in an earlier section. The dynamic response reveals information such as heating and cooling rates and allows one to determine maximum deflection attainable at a particular actuation cycle rate.

7.1 Methods

The characterization of the dynamic response was done with a Polytec Micro System Analyzer using stroboscopic video feature tracking. Two current levels from the previous testing were selected for each of the types of actuators for the dynamic testing. The Polytec system allowed control only of voltage, so nominal voltage levels were determined corresponding to the current levels desired. Square-wave signals with these voltage amplitudes were sent to the thermal actuators, and the motion of the actuators was captured stroboscopically over many periods. The period of the square wave was selected so that the thermal actuators reached approximately steady state displacement during each heating and cooling cycle. All of the available parts were sampled in this manner.

7.2 Results

The raw data collected in the test were stroboscopic movies of the thermal actuators through 1.5 cycles of actuation and cooling. Figure 18 shows a series of images taken from one of the movies collected of the heating cycle for a P123 thermal actuator. Feature tracking was used to find the displacement of the thermal actuator shuttle as a function of time, and FFT analysis was performed on the results.

For the majority of tests, a 200 Hz 50% duty cycle square wave input was used at two voltages that were chosen to give approximately 12 A and 15 A through the actuators. These two currents were chosen to be representative of typical operating conditions but, since the test apparatus does not allow current control, approximate voltages had to be used, so the actual current was measured. Feature tracking was used to generate the displacement time histories for the P123 devices tested shown in Figure 19. In one of the early tests, a faster square wave was used, but it was quickly decided that the actuator would get closer to steady state if the input square wave was slightly slower. The #5 device shows a displacement that is significantly lower than the rest of the devices in the figure. This device is one of the ones used previously for temperature measurements shown in an earlier section. For those tests, it was held in an actuated state for a long time. It appears that this earlier testing degraded the actuator performance significantly relative to the pristine actuators.

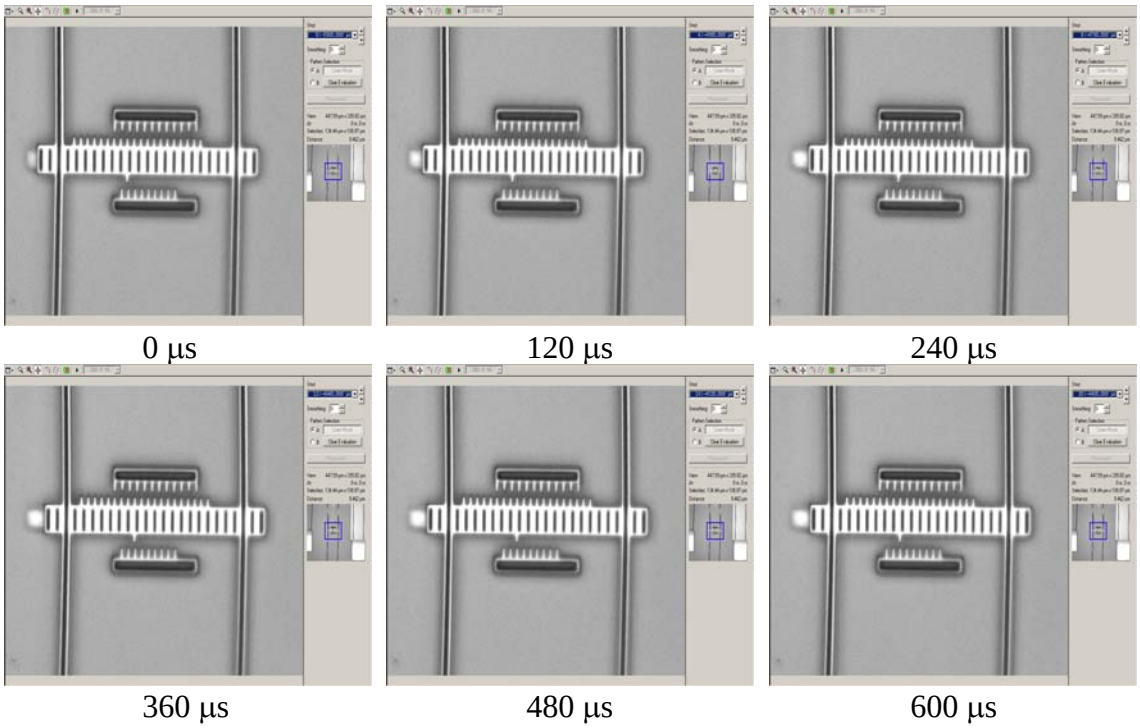

Figure 18: Snap shots of the P123 thermal actuator motion during a heating cycle

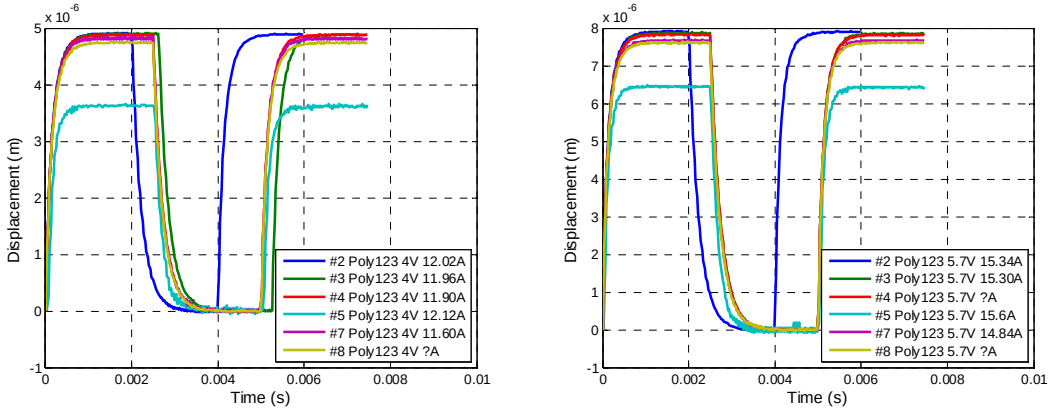

Figure 19: Time histories of displacement for P123 actuators with a 200 Hz 50% duty cycle square wave input (except in one case where it was a 250 Hz square wave) at two voltages

To get a sense for the time constant involved in the displacement of the actuator during heating FFTs were taken of the first heating cycle shown in Figure 19. The results are shown in Figure 20. Figure 21 shows a comparison of FFT results from a heating cycle and a cooling cycle in comparison. It appears that the time constant for the cooling phase is slightly slower than for the heating. This indicates that a drive signal with a 50% duty cycle will increase the mean temperature of the device. A drive signal with a duty cycle somewhat less than 50%, however, can be found that will not produce a destructive mean heating. Similar results are shown in Figure 22 to Figure 24 for the P123F actuators with an integrated force gauge and Figure 25 to Figure 27 for the P34 actuators. In a few cases during testing, the current resulting from the voltage across the actuators was not recorded. This is indicated by a ?A in the figures.

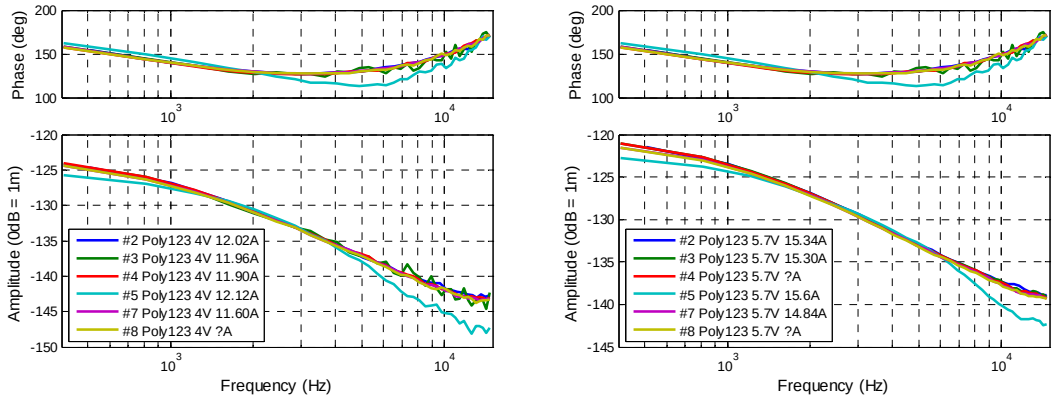

Figure 20: FFT of the heating cycle for P123 actuators (typically the first 0.0025 s of the data in Figure 19) at two voltages

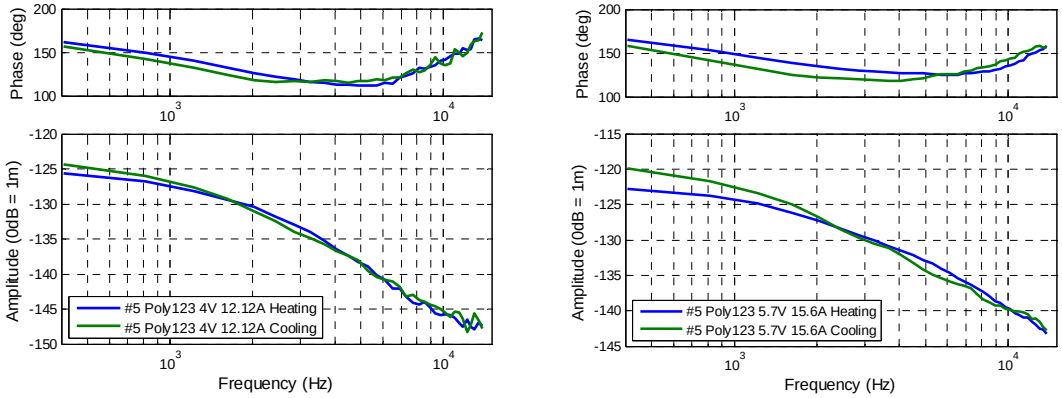

Figure 21: Typical comparison of heating and cooling cycles for one of the P123 actuators tested at two voltages

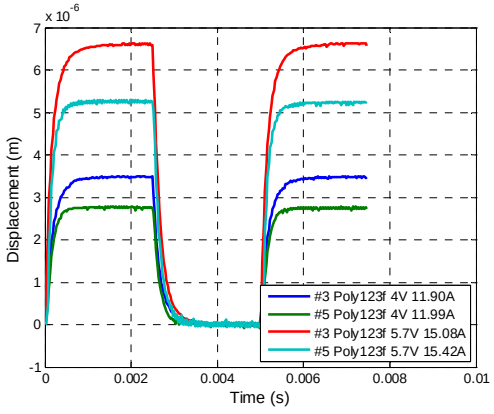

Figure 22: Time histories of displacement for P123F actuators with a 200 Hz 50% duty cycle square wave input at two voltages

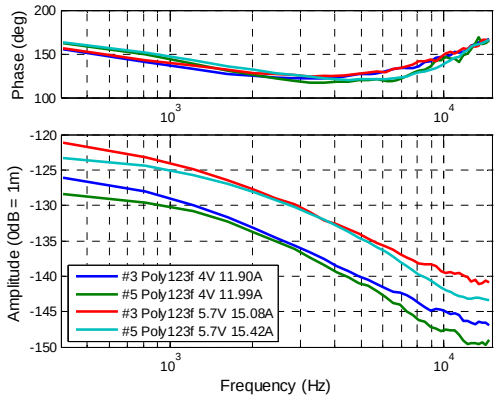

Figure 23: FFT of the heating cycle for P123F actuators (typically the first 0.0025 s of the data in Figure 22) at two voltages

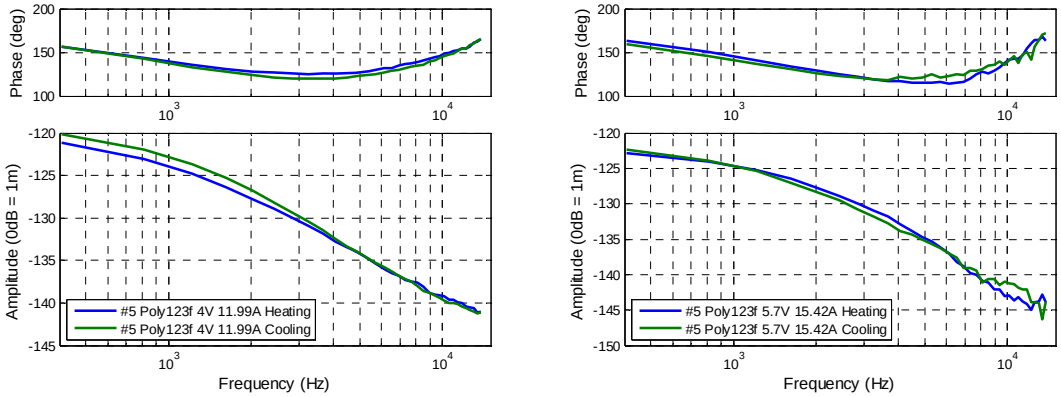

Figure 24: Typical comparison of heating and cooling cycles for one of the P123 actuators with force gauges tested at two voltages

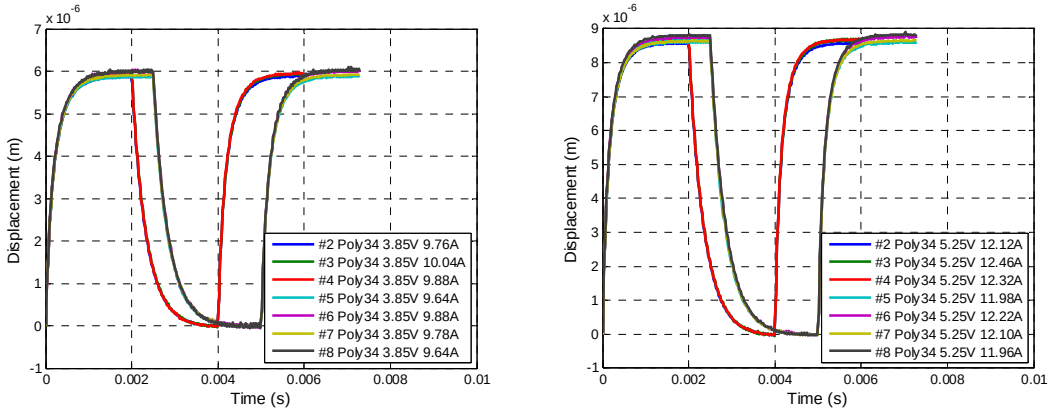

Figure 25: Time histories of displacement for P34 actuators with a 200 Hz 50% duty cycle square wave input (except in two cases where it was a 250 Hz square wave) at two voltages

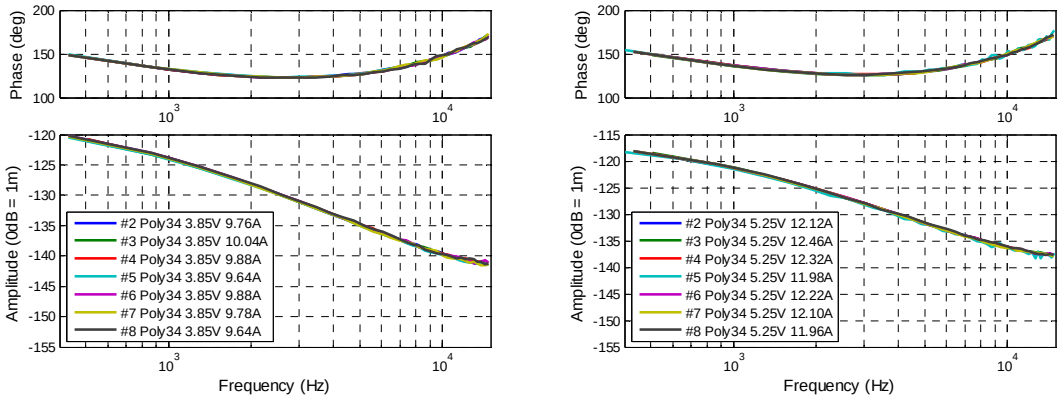

Figure 26: FFT of the heating cycle for P34 actuators (typically the first 0.0025 s of the data in Figure 25) at two voltages

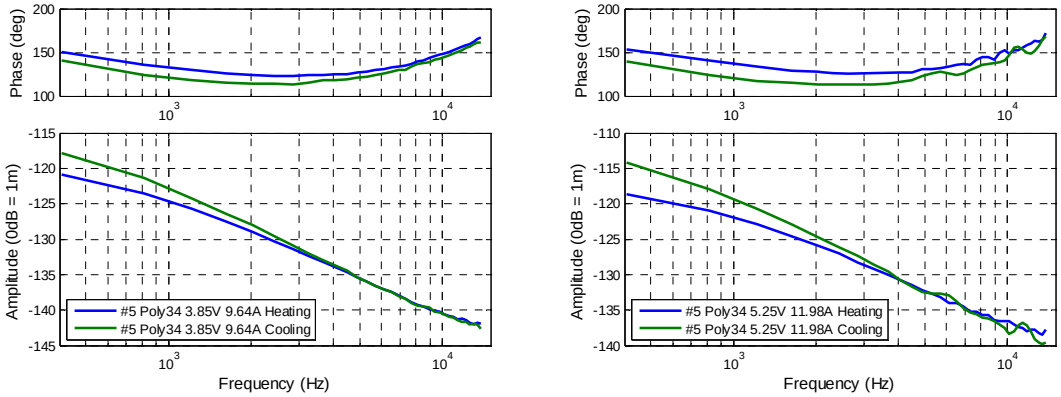

Figure 27: Typical comparison of heating and cooling cycles for one of the P34 actuators tested at two voltages

8. Conclusions

Fundamental physical understanding and model validation are key steps in the development of predictive simulation capabilities for microsystems. While in macroscale systems the thermal and mechanical behavior may be measured and analyzed independently, thermal and mechanical phenomena are strongly coupled in MEMS. This coupling is both advantageous as it enables thermally activated microactuators to function through thermal expansion of heated members and also presents challenges such as out-of-plane deformation effects that can impact thermal microactuator reliability. Both experimental and modeling research efforts on MEMS actuators are reported in the literature. Although experimental thermal and mechanical data for thermal microactuators exist, a full suite of thermal and mechanical measurements was not available for a given microactuator design. Thermal and mechanical measurements for three bent-beam polysilicon thermal microactuators are reported.

8.1 Summary of Results

Thermal and mechanical measurements for bent-beam polycrystalline silicon thermal microactuators are reported, including displacement, overall actuator electrical resistance, force, temperature profiles along microactuator legs in standard laboratory air pressures and reduced pressures down to 50 mTorr, resonant frequency, out-of-plane displacement, and dynamic displacement response to applied voltages. The electrical and thermal measurements exhibit the effect of increasing gap thickness under a microactuator in creating higher temperatures due to decreasing energy transfer through the underlying gas. Decreasing the pressure in which the thermal microactuators are operated moves the location of maximum temperature from about two-thirds of the distance between the anchor and shuttle to being on the shuttle. At low pressures, the shuttle does not function as a heat sink since it is not able to transfer the energy to substrate. Resonant frequencies were measured for P34 and P123F microactuators, but the high-speed camera resolution was not sufficient to record the P123 resonant frequency. Out-of-plane motions were observed; however, the test results were not consistent, leading to model validation challenges. The dynamic displacement response measurements confirm that the cooling phase is longer than the heating phase and limits the switching speed. Also, a difference in the dynamic response was observed between tested and pristine parts.

8.2 Recommendations for Future Work

A Campaign 6 project investigating thermomechanical phenomena in microsystems developed diagnostic techniques and collected data to illuminate fundamental physical phenomena and for model validation. To further advance SNL microsystems programs, several avenues for future work are suggested by the project results. The available resources, experimental development efforts, and range of experiments limited the number of parts examined and tests performed. Testing more parts improves data statistics and may reveal phenomena or trends that a smaller number of tests did not observe. Specifying the measurements which are most useful for model validation would focus future experimental efforts and facilitate the collection of better test statistics. Also, the present results are primarily for thermal microactuators that were operated under standard conditions. More experiments are needed that investigate and focus on failure

mechanisms such as the permanent deformation of thermal microactuator legs after being operated at higher currents. Model validation data do not yet exist for this phenomenon. Further exploration of environmental and operating effects on micromachined materials and devices is needed to understand issues like the change in the observed dynamic response between tested and pristine thermal microactuators. Due to the sensitivity of simulation results to device dimensions and material properties, practical methods of monitoring these quantities for fabricated parts and providing them for analysis and simulation would advance the development of predictive simulation capabilities for microsystems. Also, several microsystems devices are now being designed and fabricated using silicon on insulator (SOI) techniques, and efforts need to be initiated to understand, characterize, test, and provide validation data for SOI parts.

9. References

Ataka et al., 1993: M. Ataka, A. Omodaka, N. Takeshima, and H. Fujita, "Fabrication and Operation of Polyimide Bimorph Actuators for a Ciliary Motion System," *Journal of Microelectromechanical Systems*, Vol. 2, pp. 146-150, 1993.

Baker et al., 2004: M. S. Baker, R. A. Plass, T. J. Headley, and J. A. Walraven, "Final Report: Compliant Thermomechanical MEMS Actuators LDRD #52553," Sandia report SAND2004-6635, Sandia National Laboratories, Albuquerque, NM, 2004.

Calore, 2006: S. W. Bova, K. D. Copps, and C. K. Newman, "Calore: A Computational Heat Transfer Program, Volume 1: Theory Manual," Sandia report SAND2006-6083P, Sandia National Laboratories, Albuquerque, NM, 2006.

Calore, 2008: Calore Development Team, "Calore: A Computational Heat Transfer Program, Volume 2: User Reference Manual," Version 4.6, Sandia report SAND2008-0098P, Sandia National Laboratories, Albuquerque, NM, 2008.

Comtois et al., 1998: J. H. Comtois, M. A. Michalicek, and C. C. Barron, "Electrothermal Actuators Fabricated in Four-Level Planarized Surface Micromachined Polycrystalline Silicon," *Sensors and Actuators A*, Vol. 70, pp. 23-31, 1998.

Enikov et al., 2005: E. T. Enikov, S. S. Kedar, and K. V. Lazarov, "Analytical Model for Analysis and Design of V-Shaped Thermal Microactuators," *Journal of Microelectromechanical Systems*, Vol. 14, pp. 788-798, 2005.

Hickey et al., 2003: R. Hickey, D. Sameoto, T. Hubbard, and M. Kujath, "Time and Frequency Response of Two-Arm Micromachined Thermal Actuators," *Journal of Micromechanics and Microengineering*, Vol. 13, pp. 40-46, 2003.

Kearney et al., 2006a: S. P. Kearney, J. R. Serrano, L. M. Phinney, S. Graham, T. Beecham, and M. R. Abel, "Noncontact Surface Thermometry for Microsystems: LDRD Final Report," Sandia report SAND2006-6369, Sandia National Laboratories, Albuquerque, NM, 2006.

Kearney et al., 2006b: S. P. Kearney, L. M. Phinney, and M. S. Baker, "Spatially Resolved Temperature Mapping of Electrothermal Actuators by Surface Raman Scattering," *Journal of Microelectromechanical Systems*, Vol. 15, pp. 314-321, 2006.

Lott et al., 2002: C. D. Lott, T. W. McLain, J. N. Harb, and L. L. Howell, "Modeling the Thermal Behavior of a Surface-Micromachined Linear-Displacement Thermomechanical Microactuator," *Sensors and Actuators A*, Vol. 101, pp. 239-250, 2002.

Mankame and Ananthasuresh, 2001: N. D. Mankame and G. K. Ananthasuresh, "Comprehensive Thermal Modelling and Characterization of an Electro-Thermal-Compliant Microactuator," *Journal of Micromechanics and Microengineering*, Vol. 11, pp. 452-462, 2001.

Oliver et al., 2003: A. D. Oliver, S. R. Vigil, and Y. B. Gianchandani, "Photothermal Surface-Micromachined Actuators," *IEEE Transactions on Electron Devices*, Vol. 50, pp. 1156-1157, 2003.

Park et al., 2001: J.-S. Park, L. L. Chu, A. D. Oliver, and Y. B. Gianchandani, "Bent-Beam Electrothermal Actuators – Part II: Linear and Rotary Microengines," *Journal of Microelectromechanical Systems*, Vol. 10, pp. 255-262, 2001.

Que et al., 2001: L. Que, J.-S. Park, and Y. B. Gianchandani, "Bent-Beam Electrothermal Actuators – Part I: Single Beam and Cascaded Devices," *Journal of Microelectromechanical Systems*, Vol. 10, pp. 247-254, 2001.

Serrano et al., 2006: J. R. Serrano, L. M. Phinney, and S. P. Kearney, "Micro-Raman Thermometry of Thermal Flexure Actuators," *Journal of Micromechanics and Microengineering*, Vol. 16, pp. 1128-1134, 2006.

Sinclair et al., 2005: M. B. Sinclair, M. P. de Boer, and A. D. Corwin, "Long-Working-Distance Incoherent Light Interference Microscope," *Applied Optics*, Vol. 44, pp. 7714-7721, 2005.

Sniegowski and de Boer, 2000: J. J. Sniegowski and M. P. de Boer, "IC-Compatible Polysilicon Surface Micromachining," *Annual Review of Materials Science*, Vol. 30, pp. 299-333, 2000.

SUMMiT V, 2008: SUMMiT V™ Five Level Surface Micromachining Technology Design Manual, Version 3.1a, Sandia report SAND2008-0659P, Sandia National Laboratories, Albuquerque, NM, 2008.

Torczynski et al., 2008: J. R. Torczynski, M. A. Gallis, E. S. Piekos, J. R. Serrano, L. M. Phinney, and A. D. Gorby, "Validation of Thermal Models for a Prototypical MEMS Thermal Actuator," Sandia report SAND2008-5749, Sandia National Laboratories, Albuquerque, NM, 2008.

Wong and Phinney, 2007: C. C. Wong and L. M. Phinney, "Computational Analysis of Responses of Micro Electro-Thermal Actuators," IMECE2007-41462, American Society of Mechanical Engineers, New York, NY, pp. 1-9, 2007.

DISTRIBUTION

1	MS 0346	D. J. Rader	Org. 01513	
1	MS 0346	M. A. Gallis	Org. 01513	
1	MS 0346	P. E. Hopkins	Org. 01513	
3	MS 0346	L. M. Phinney	Org. 01513	
1	MS 0346	E. S. Piekos	Org. 01513	
1	MS 0346	J. R. Serrano	Org. 01513	
1	MS 0346	J. R. Torczynski	Org. 01513	
1	MS 0372	J. M. Redmond	Org. 01525	
1	MS 0824	T. Y. Chu	Org. 01500	
1	MS 0833	C. L. Northrop	Org. 01055	
1	MS 1064	J. B. Wirth	Org. 02614	
1	MS 1064	E. J. Garcia	Org. 02614	
1	MS 1069	M. S. Baker	Org. 017492	
1	MS 1069	M. R. Platzbecker	Org. 017491	
1	MS 1069	D. M. Tanner	Org. 017491	
1	MS 1070	C. C. Wong	Org. 01526	
1	MS 1070	D. S. Epp	Org. 01526	
1	MS 1070	H. Sumali	Org. 01526	
1	MS 1080	M. J. Shaw	Org. 017491	
1	MS 0899	Technical Library	Org. 09536	(electronic copy)


Sandia National Laboratories